Atmospheric
Chemistry
and Physics

Investigations of temporal and spatial distribution of precursors SO₂ and NO₂ vertical columns in the North China Plain using mobile DOAS

Fengcheng Wu[1], Pinhua Xie[1,3,4], Ang Li[1], Fusheng Mou[1], Hao Chen[1], Yi Zhu[2], Tong Zhu[2], Jianguo Liu[1], and Wenqing Liu[1]

[1]Key Laboratory of Environmental Optical and Technology, Anhui Institute of Optics and Fine Mechanics,
Chinese Academy of Sciences, Hefei, 230031, China
[2]State Key Laboratory of Environmental Simulation and Pollution Control, College of Environmental Sciences
and Engineering, Peking University, Beijing, 100871, China
[3]Center for Excellence in Regional Atmospheric Environment, Institute of Urban Environment,
Chinese Academy of Sciences, Xiamen, 361021, China
[4]School of Environmental Science and Optoelectronic Technology, University of Science and Technology of China,
Hefei, 230026, China

Correspondence: Pinhua Xie (phxie@aiofm.ac.cn)

Abstract. Recently, Chinese cities have suffered severe events of haze air pollution, particularly in the North China Plain (NCP). Investigating the temporal and spatial distribution of pollutants, emissions, and pollution transport is necessary to better understand the effect of various sources on air quality. We report on mobile differential optical absorption spectroscopy (mobile DOAS) observations of precursors SO₂ and NO₂ vertical columns in the NCP in the summer of 2013 (from 11 June to 7 July) in this study. The different temporal and spatial distributions of SO₂ and NO₂ vertical column density (VCD) over this area are characterized under various wind fields. The results show that transport from the southern NCP strongly affects air quality in Beijing, and the transport route, particularly SO₂ transport on the route of Shijiazhuang–Baoding–Beijing, is identified. In addition, the major contributors to SO₂ along the route of Shijiazhuang–Baoding–Beijing are elevated sources compared to low area sources for the route of Dezhou–Cangzhou–Tianjin–Beijing; this is found using the interrelated analysis between in situ and mobile DOAS observations during the measurement periods. Furthermore, the discussions on hot spots near the city of JiNan show that average observed width of polluted air mass is 11.83 and 17.23 km associated with air mass diffusion, which is approximately 60 km away from emission sources based on geometrical estimation. Finally, a reasonable agreement exists between the Ozone Monitoring Instrument (OMI) and mobile DOAS observations, with a correlation coefficient (R^2) of 0.65 for NO₂ VCDs. Both datasets also have a similar spatial pattern. The fitted slope of 0.55 is significantly less than unity, which can reflect the contamination of local sources, and OMI observations are needed to improve the sensitivities to the near-surface emission sources through improvements of the retrieval algorithm or the resolution of satellites.

1 Introduction

Driven by the unprecedented economic growth and explosive increase in urbanization, China has been experiencing severe air pollution, particularly in developed areas, such as the Yangtze River Delta region and Pearl River Delta region (van Donkelaar et al., 2010). Severe haze pollution events have occurred frequently since the end of 2012 in the Jing-Jin-Ji region, including Beijing, Tianjin, Shijiazhuang, and some cities in Hebei Province. Long duration, heavy pollution level, and large spread area are the main characteristics of haze pollution, which used to be rare in past decades (Sun

et al., 2014; Ji et al., 2014; X. J. Zhao et al., 2013). Haze pollution has affected the health and lifestyle of millions, drawing extensive worldwide attention to China. Severe air pollution in Beijing, the capital of China, has troubled the public, scholars, and the government. Concurrently, many studies have been conducted in Beijing and its surrounding areas (Y. S. Wang et al., 2014; Z. F. Wang, 2014; Xu et al., 2011; Ma et al., 2012). Related results show that the air pollution in Beijing is a regional environmental problem caused by the influences of both local emissions and external transport (Ying et al., 2014; Guo et al., 2014; Wu et al., 2011).

NO_2 is one of the most important atmospheric trace gases. It plays a key role in tropospheric and stratospheric chemistry and strongly participates in the chain reaction formation of tropospheric ozone (Crutzen et al., 1970). Moreover, NO_2 is the main pathway of OH loss, which determines the atmospheric oxidative capacity under heavy polluted conditions (Finlayson-Pitts et al., 1999; Kanaya et al., 2014). Aside from NO_2 being generally harmful to human health, long-term NO_2 exposure in high concentrations can also increase the possibility of bronchitis in asthmatic children (WHO, 2006). Combustion processes, such as power generation and release of pollutants from vehicles, are major sources of anthropogenic NO_2 emissions. Meanwhile, SO_2 is a colorless gas that adversely affects the respiratory system. Emissions from elevated releases, such as from power plants, are the main contributors for anthropogenic SO_2 emission (Xu et al., 1998; Ramanathan et al., 2003). Furthermore, NO_2 and SO_2 are important precursors of aerosol. Under suitable meteorological conditions, NO_2 and SO_2 tend to form nitrate and sulfate, which contribute to the formation of secondary aerosols (Jang et al., 2001; Boichu et al., 2015). Some studies show that nitrate and sulfate account for nearly 38 % in particulate matter ($PM_{2.5}$, with aerodynamic diameter less than or equal to 2.5 μm), which is an important element of haze in the Jing-Jin-Ji region (Huang et al., 2014; Yang et al., 2011; Sun et al., 2013; Zhang et al., 2013). Based on model simulation, $PM_{2.5}$ concentration can be reduced by 13 % if SO_2 and NO_x emission are controlled effectively (B. Zhao et al., 2013). In addition, the spatial and temporal distribution of SO_2 and NO_x (nitrogen oxides, sum of NO and NO_2, $NO_x = NO + NO_2$) vary significantly (Lee et al., 2009; Matsui et al., 2009; Wang et al., 2009). To investigate the spatial and temporal distribution of SO_2 and NO_2 and to evaluate the influence of transport on Beijing, the observations of distribution of tropospheric SO_2 and NO_2 vertical column densities (VCDs) were conducted in the North China Plain (NCP) using mobile differential optical absorption spectroscopy (DOAS) from June to July 2013. The NCP is located in northern China, surrounded by Taihang Mountains (to the west of the NCP), Yanshan Mountains (to the north of the NCP) and Bohai Sea (to the east of the NCP). The NCP consists of the Jing-Jin-Ji region and other provinces in northern China and is one of the heaviest polluted areas in China (Quan et al., 2011).

A large number of studies on distributions of air pollutants have been performed in the NCP. The characteristics of concentration and evolution at different sites and formation mechanisms during heavy pollution periods have been researched using ground-based observation networks (Hu et al., 2014). Meanwhile, regional variation of gases, particle pollutants, and other factors which influence pollution characteristics has been detected using airborne measurement (Zhang et al., 2014). Also, based on measurements using a mobile laboratory, Wang et al. (2011) analyzed the regional distribution of SO_2 in Beijing and its surrounding areas and estimated transport flux from the outside to Beijing (Wang et al., 2011). Model simulations, another method, can obtain distribution, transboundary transport fluxes, and major transport channels of Beijing in combination with meteorological data (An et al., 2012). However, current studies mainly focus on ground-based observations, lacking stereoscopic monitoring data that can help better understand the source and transport of air pollution.

Mobile DOAS provides another remote sensing method to obtain stereoscopic monitoring data and characterize the regional distribution of air pollution over a medium- to long-distance scale. This technique can detect the horizontal distribution of pollutants with high spatial–temporal resolution and rapidly identify the locations of pollution sources. Furthermore, information on the upper layer of air pollution can be investigated. Thus, the transport of air pollution can be analyzed and associated with meteorological trajectory data. At present, some related studies have been carried out (Ibrahim et al., 2010; Shaiganfar et al., 2011, 2015). In China, several measurements are also performed in Shanghai and Guangzhou. Wang et al. (2012) evaluated NO_2 variation over the central urban area before and after the Shanghai Expo 2010 (Wang et al., 2012). Wu et al. (2013) observed the distributions and emissions of SO_2 and NO_2 in the eastern area of Guangzhou during the Guangzhou Asian Games 2010 (Wu et al., 2013). However, this study aims to summarize the distributions of SO_2 and NO_2, verify the type of air pollution sources, and discuss the potential of transport from the NCP to Beijing over the NCP area. In addition, the mobile platform referred to in this study is also equipped with some in situ instruments from Peking University (PKU) to synchronously measure near-surface concentration of gases and particulate mass.

In this paper, we present the observations of SO_2 and NO_2 VCDs in the NCP from June to July 2013 using mobile DOAS, and the distributions of SO_2 and NO_2 VCDs in the NCP are characterized. In combination with in situ data, the characteristics of SO_2 and NO_2 along southwest and southeast pathway under different wind fields are characterized, and the hot spots and their possible sources along the measurement paths are determined. The pollution transport pathways to Beijing are revealed and confirmed for the first time by capturing the plume. Finally, the NO_2 VCDs from mobile DOAS data are compared with those from the Ozone Mon-

itoring Instrument (OMI). Data obtained are in good agreement.

This paper is organized as follows: the experimental process, including an overview of the measurements and instruments, is given. Wind fields and the principle of retrieval of vertical column densities of tropospheric trace gases are discussed in detail in Sect. 2. Section 3 gives us the results and discussions, including distributions of SO$_2$ and NO$_2$ tropospheric VCDs over NCP and the analysis of hot spots and the comparison with OMI NO$_2$. Finally, the conclusions are presented in Sect. 4.

2 Experimental

2.1 Overview of the measurements

To characterize spatial distributions of SO$_2$ and NO$_2$ VCDs and investigate potential transport to Beijing, the measurement routes are specially designed. The entire measurement period from 11 June to 16 July 2013 is initially divided into five identical cycles. Mobile DOAS observations span four cycles (from 11 June to 7 July) and cover four different routes because of bad weather or vehicle problems. Figure 1 depicts the detailed routes of mobile DOAS measurements. Cycle 1 covers five routes with a total path of 1400 km and takes 5 days to complete. The five routes are Beijing (BJ) to Shijiazhuang (SJZ), Shijiazhuang to Dezhou (DZ), Dezhou to Baoding (BD) to Cangzhou (CZ), Cangzhou to Zhuozhou (ZZ), and Zhuozhou to Beijing for Cycle 1. Due to bad weather or vehicle problems, Cycles 2 and 3 took 4 and 3 days to complete, respectively, resulting in some routes being skipped. We needed 1 more day to complete Cycle 4 due to power failure on 4 July. The details of monitoring information are listed in Table 1.

The approximate starting and ending times are 10:00 and 14:00 (local time, LT), particularly considering stable boundary layer and battery endurance. The temperature varied from 30 to 36 °C and the wind fields were dominated by south and north. Some other meteorological parameters, e.g., humidity and pressure, are in the range of 32–61 % and 994–1009 hPa during the entire measurement period.

2.2 Instrument description

The mobile DOAS instrument collects scattered sunlight from zenith observations. Details of the instrument and performances are described in our previous study (Wu et al., 2013). Briefly, the system consists of telescope, a miniature fiber spectrometer unit, a global positioning system, and a computer. The series of Ocean Optics HR2000 is selected as the miniature spectrometer, with a spectral resolution of 0.6 nm and a spectral range of 290 to 420 nm. The spectrometer is stored in a temperature-controlled unit to stabilize the temperature at +30 ± 0.1 °C to avoid spectral shifts caused by temperature variation. The detection limits of the instru-

ment are approximately 3–5 × 10^{15} molec. cm^{-2} for SO$_2$ and NO$_2$. The instrument is installed on a van, which is a mobile laboratory platform from PKU (Wang et al., 2009, 2011). The mobile DOAS system is powered by a 220 V alternating current through conversion of a +12 V direct current battery with a power converter.

In addition, PKU has set up some in situ instruments on the van, including an SO$_2$ analyzer (ECOTECH 9850A), an NO$_x$ analyzer (ECOTECH 9841A), a CO analyzer (ECOTECH 9830A), an ozone analyzer (ECOTECH 9810A), and a CO$_2$ analyzer (ECOTECH 9820A). Aside from gaseous pollutant instruments, some aerosol instruments, such as GRIMM and Dusttrak for PM$_{2.5}$ and a Fast Mobility Particle Sizer, were also available on board for analysis of particle size distribution. The details of the setup and performance of the instruments are described in Wang et al. (2009, 2011).

2.3 Backward Lagrangian trajectory simulation

Apart from the near-surface wind data, the backward trajectory of air mass from the stations in Beijing was also simulated using the Hybrid Single Particle Lagrangian Integrated Trajectory model (HYSPLIT, offline version), which has been developed by the Air Resources Laboratory of the US National Oceanic and Atmospheric Administration. An average boundary layer height (BLH) of around 1000 m was calculated during noontime in summer over the NCP area by Lv et al. (2017), based on lidar observations. The middle altitude of BLH, i.e., 500 m, is taken as the representative horizontal transport height to investigate the transport effect, with an assumption of well mixing throughout the whole BLH around noontime. Backward trajectories were calculated once every 2 h for 1 day (24 h) at a selected altitude of 500 m a.g.l. for each cycle. An archive meteorological database with a horizontal resolution of 1° × 1° from the Global Data Assimilation System, which is enough to identify the original regions of air mass, is chosen to run the HYSPLIT model.

Figure 2 shows the cluster average backward trajectory for Cycles 1, 2, 3, and 4. During the measurement periods of Cycles 1 and 3, all air masses come from the southern regions. For Cycle 2, the mean back trajectory is roughly split equally between north and south. However, the dominant wind field is north during the mobile DOAS observations for Cycle 2, except for the wind on 21 June as listed in Table 1. A slightly different wind field is present for Cycle 4. The north wind accounts for nearly 72 % and the south wind 28 %. There are maybe some differences from the wind data as listed in Table 1 for Cycle 4. Two main reasons could account for the differences. Firstly, the backward trajectories are simulated at the Beijing site, and this ratio represents the Beijing area. Secondly, the ratio results from calculations of 60 trajectories in 5 days for Cycle 4. However, the wind data described in Table 1 focus on the time period of mobile DOAS observations. In general the wind fields show variation in the
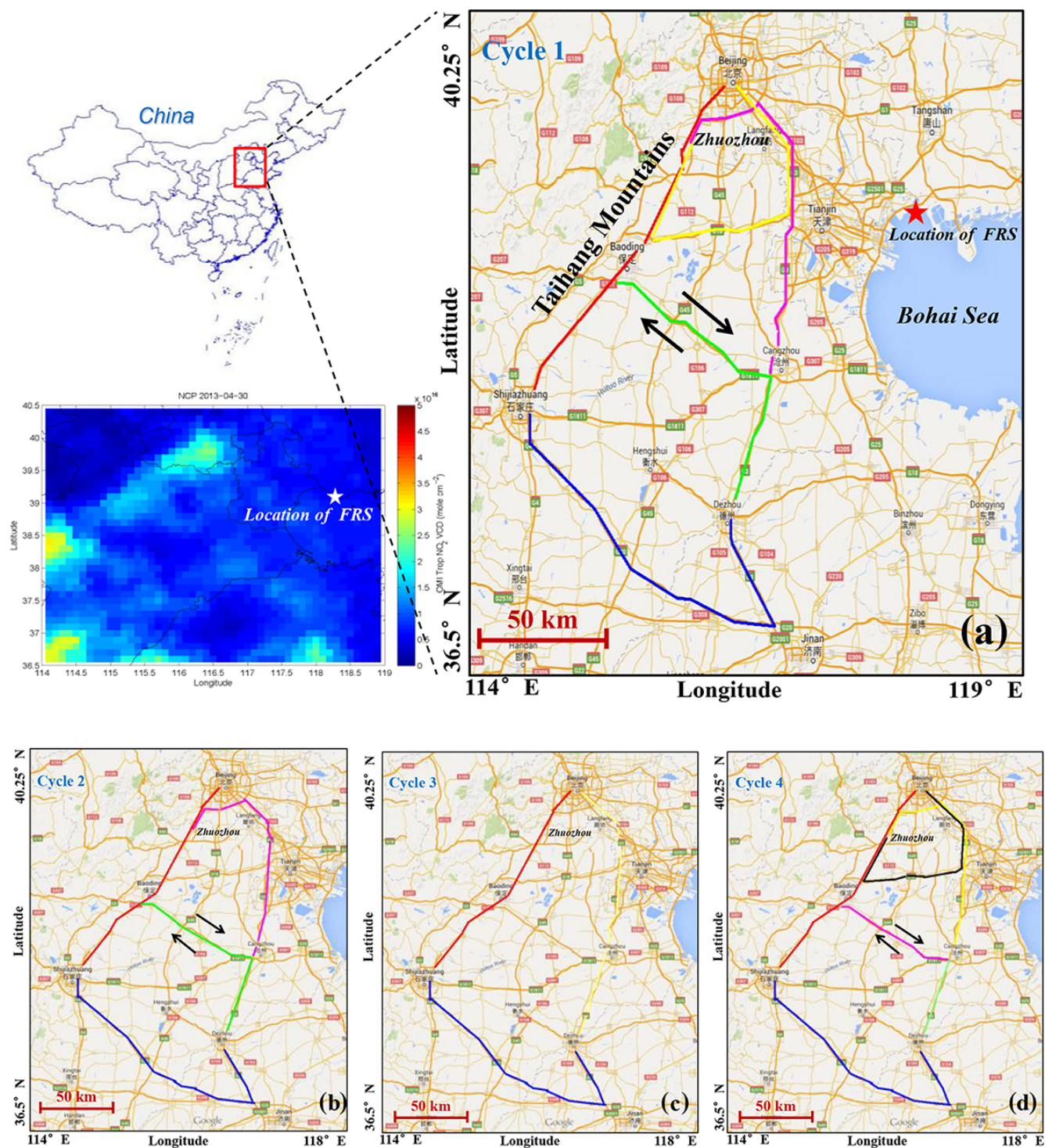
Figure 1. Maps of the mobile measurement areas and routes. The red, blue, green, pink, and yellow tracks show the routes of BJ–SJZ, SJZ–DZ, DZ–BD–CZ, CZ–ZZ, and ZZ–BJ **(a)**. The OMI NO_2 VCD on 30 April shows that the NO_2 VCD of FRS is low **(a)**. Panel **(a)** also marks the location of FRS, the Bohai Sea, and Taihang Mountains. The red, blue, green, and pink tracks indicate the routes of BJ–SJZ, SJZ–DZ, DZ–BD–CZ, and CZ–ZZ **(b)**. The red, blue, and yellow tracks show the routes of BJ–SJZ, SJZ–DZ, and DZ–BJ **(c)**. The red, blue, green, pink, yellow, and black tracks show the routes of BJ–SJZ, SJZ–DZ, DZ–CZ, CZ–BD–CZ, CZ–ZZ, and ZZ–BJ **(d)**. The black arrows indicate the monitoring route from CZ to BD and the return to CZ.

Table 1. Summary of monitoring information of mobile DOAS. Wind data are from airport meteorological data: http://www.wunderground. com. The wind data indicate the wind field at the time of mobile DOAS measurement.

Cycles	Date	Time (LT)	Routes	Wind direction	Wind speed (m s^{-1})
	11 Jun	10:14–14:00	BJ-SJZ	BJ: southeast	BJ: 2–3
				SJZ: southwest	SJZ: 1–2
	12 Jun	10:24–14:05	SJZ-DZ	SJZ: southwest	SJZ: 1–2
				DZ: southwest	DZ: 3–4
Cycle 1	13 Jun	10:20–15:04	DZ-BD-CZ	DZ: southwest	DZ: 4–5
				BD: south	BD: 2–3
				CZ: southwest	CZ: 4-5
	14 Jun	10:02–13:45	CZ-ZZ	CZ: southwest	CZ: 4–5
				ZZ: southwest	ZZ: 4–5
	15 Jun	09:57–14:06	ZZ-BJ	ZZ: south	ZZ: 2–3
				BJ: south	BJ: 2
	17 Jun	10:36–14:19	BJ-SJZ	BJ: northeast	BJ: 2–3
				SJZ: northeast	SJZ: 3
	18 Jun	10:02–13:32	SJZ-DZ	SJZ: north	SJZ: 1–2
				DZ: north	DZ: 1–2
Cycle 2	20 Jun	10:25–15:05	DZ-BD-CZ	DZ: northwest	DZ: 2–3
				BD: northwest	BD: 2–3
				CZ: northeast	CZ: 3–4
	21 Jun	09:57–13:24	CZ-ZZ	CZ: west	CZ: 3–4
				ZZ: southwest	ZZ: 2–3
	24 Jun	10:47–14:06	BJ-SJZ	BJ: southeast	BJ: 2–3
				SJZ: south	SJZ: 2–3
Cycle 3	25 Jun	10:10–14:17	SJZ-DZ	SJZ: south	SJZ: 1–2
				DZ: south	DZ: 3–4
	26 Jun	09:43–14:01	DZ-BJ	DZ: southwest	DZ: 4–5
				BJ: south	BJ: 3–4
	2 Jul	10:24–14:13	BJ-SJZ	BJ: northwest	BJ: 5–6
				SJZ: northwest	SJZ: 3–4
	3 Jul	10:26–14:01	SJZ-DZ	SJZ: southwest	SJZ: 2
				DZ: southwest	DZ: 3–4
Cycle 4	4 Jul	10:12–11:54	DZ-CZ	DZ: southwest	DZ: 3–4
				CZ: southeast	CZ: 1–2
	5 Jul	09:55–13:40	CZ-BD-CZ	CZ: northeast	CZ: 3–4
				BD: northeast	BD: 3–4
	6 Jul	09:56–14:23	CZ-ZZ	CZ: southeast	CZ: 2–3
				ZZ: southwest	ZZ: 2–3
	7 Jul	10:12–13:21	ZZ-BJ	ZZ: southeast	ZZ: 2–3
				BJ: southeast	BJ: 2–3

NCP for Cycle 4, and the specific observation time of mobile DOAS shows that the south wind is dominant except for on 2 and 5 July.

2.4 Retrieval of vertical density of tropospheric trace gas

SO$_2$ and NO$_2$ column densities are retrieved from zenith sky mobile DOAS with WinDOAS software. Each measured spectrum is divided by the Fraunhofer reference spectrum (FRS) after dark current and offset corrections. One FRS spectrum, a relative "clean-air" spectrum, is selected to re-trieve all other measured spectra during the whole field campaign. The FRS is recorded at approximately 11:30 LT on 30 April 2013 near the Bohai Sea, considering strong wind and good air quality on that day (see Fig. 1a). The spectral evaluation applied to each measurement spectrum starts with dark current and offset corrections, followed by the division with a FRS spectrum. A high-pass filter is applied to the logarithm of this ratio. Differential slant column densities (DSCDs, which are relative to the value of Frauenhofer spectrum) are then obtained by fitting narrow band spectral absorption cross sections to the processed measurement spectra. Examples of fits for NO$_2$ and SO$_2$ are illustrated in Fig. 3.
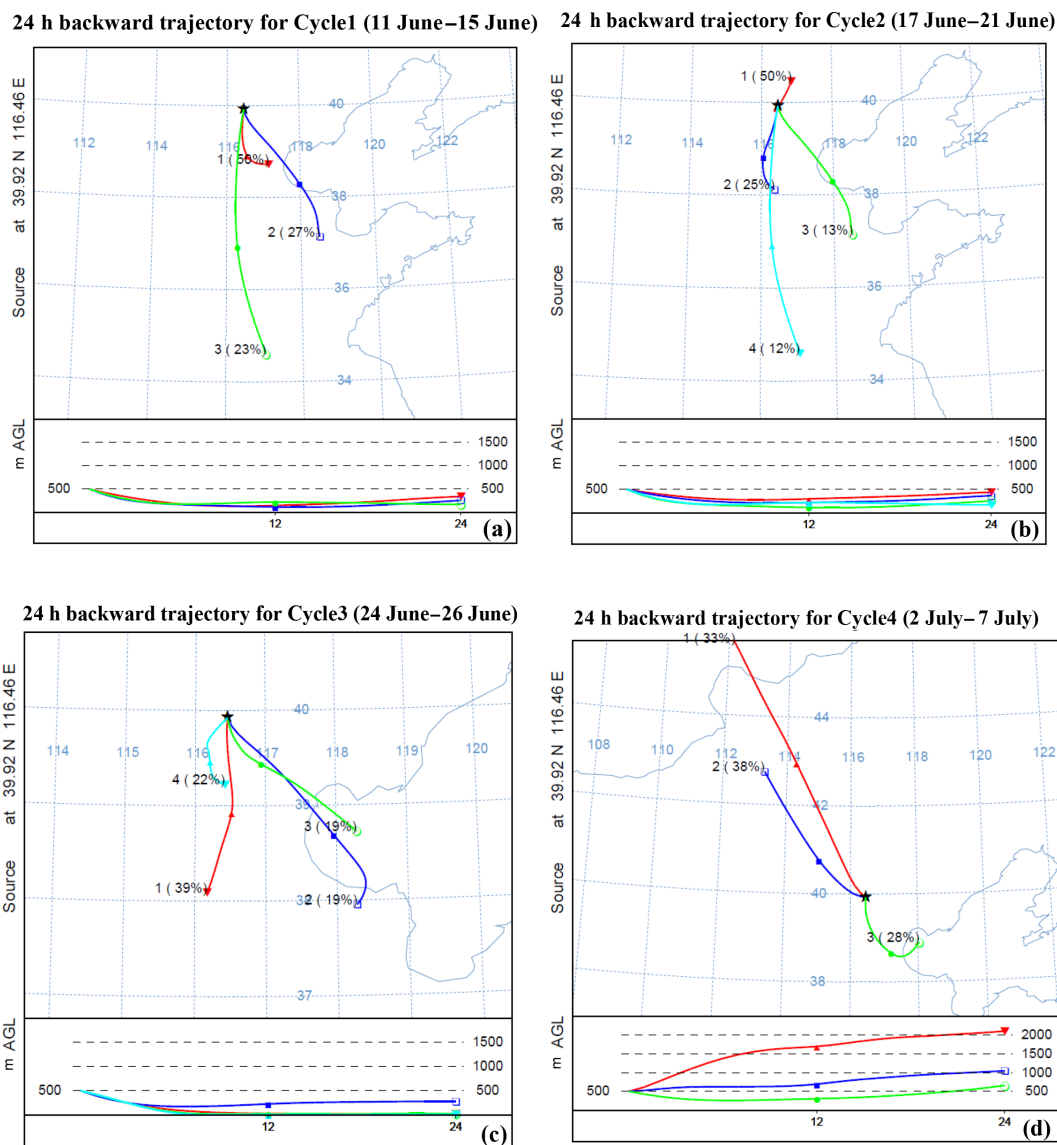
Figure 2. The 24 h cluster mean air mass backward trajectories at 500 m height at Beijing for four different cycles. The black star shows the location of Beijing. The different colored lines indicate air mass from different regions. Panels **(a)**, **(b)**, **(c)**, and **(d)** show the backward trajectory for Cycles 1, 2, 3, and 4, respectively. The percentages suggest the ratios of air mass in one region.

For the retrieval of SO$_2$, a fitting window of 310–324 nm is used and for NO$_2$, a fitting window of 338–370 nm is used, both adapted from experiences during our previous work (Wu et al., 2013) and the MAD-CAT (http://joseba.mpch-mainz.mpg.de/mad_cat.htm) intercomparison campaign. The synthetic ring spectrum is yielded from the FRS spectrum using DOASIS software (Kraus, 2006). The slit function is generated from an emission peak of a mercury lamp at 334 nm. The high-resolution solar spectrum (Kurucz et al., 1984) is used to calibrate wavelength. The setting and fitting absorbers are summarized in detail in Table 2. The fit uncertainties of NO$_2$ and SO$_2$ for the spectrum, as shown in

Fig. 3, are approximately 2.48 and 1.84 %. The typical uncertainties are less than 15 % for NO$_2$ and 20 % for SO$_2$.

The above describes how the DSCDs are obtained with respect to the FRS spectrum. Tropospheric NO$_2$ is $\sim 5 \times 10^{15}$ molec. cm^{-2} at the location of the FRS spectrum on 30 April 2013 from the OMI result. Given the poor SO$_2$ satellite data, we checked the SO$_2$ results at ground level from a local environmental protection agency on that day. Compared with the high pollution over the NCP area, we neglected these relatively small tropospheric contents in the FRS spectrum. As a result, the tropospheric NO$_2$ and SO$_2$ VCDs can be calculated with an air mass factor (AMF) using the following

Table 2. DOAS fit settings for the retrieval of SO$_2$ and NO$_2$.

Parameter	SO$_2$ fitting	NO$_2$ fitting
Fitting window	310–324 nm	338–370 nm
Polynomial degree	4	5
Intensity offset	Constant	Constant
SO$_2$	293 K (Bogumil et al., 2003)	–
NO$_2$	298 K (Vandaele et al., 1996)	298 K and 220 K (Vandaele et al., 1996)
HCHO	297 K (Meller and Moortgat, 2000)	297 K (Meller and Moortgat, 2000)
O$_3$	293 K (Bogumil et al., 2003)	223 K and 243 K (Bogumil et al., 2003)
O$_4$	–	293 K (Thalman and Volkamer, 2013)
Ring	Calculation from FRS with DOASIS	Calculation from FRS with DOASIS
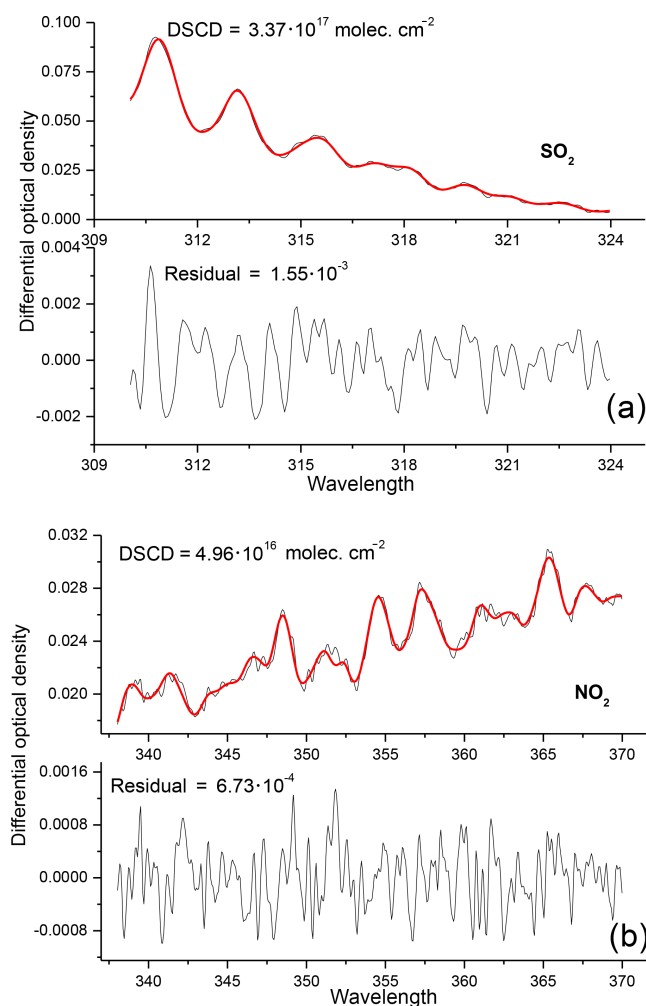
Figure 3. Example of SO$_2$ **(a)** and NO$_2$ **(b)** DSCD fits recorded at 13:04 LT on 12 June 2013. Black lines denote the differential optical densities (DODs) of the measured spectrum, and red lines show the fit results. The DSCD is the SCD (slant column density) with respect to the FRS spectrum.

formula (Hönninger et al., 2004):

$$
\begin{aligned}
\text{VCD}_{\text{trop}} &= \frac{\text{SCD}_{\text{trop}}}{\text{AMF}_{\text{trop}}} = \frac{\text{DSCD} + \text{SCD}_{\text{FRS}} - \text{SCD}_{\text{strat}}}{\text{DAMF} + \text{AMF}_{\text{FRS}} - \text{AMF}_{\text{strat}}} \\
&= \frac{\text{DSCD}_{\text{trop}}}{\text{AMF}_{\text{trop}}}.
\end{aligned}
\quad (1)
$$

The radiative transfer model McArtim (Deutschmann et al., 2011) based on the Monte Carlo method is used to calculate the AMF$_{\text{trop}}$. We assume that aerosol and trace gas profiles are homogeneous below the BLH, whereas they are exponential above the BLH. Here, the constant concentrations within 1000 m of the boundary layer are assumed to be approximately 40 and 10 ppb for NO$_2$ and SO$_2$ according to state-controlled air-sampling sites. This hypothesis can lead to less than 5 % uncertainty based on a sensitivity study by varying the setting of NO$_2$ and SO$_2$. The average aerosol optical density (AOD) of 1.0 is estimated from AERONET on June and July 2013 at the Xianghe site. The profiles of aerosol, NO$_2$, and SO$_2$ are taken from the LOWTRAN database and US Standard Atmosphere above the boundary layer. We estimate the total retrieval errors of NO$_2$ VCDs and SO$_2$ VCDs to be less than 20 and 25 % (Wu et al., 2013).

3 Results and discussions

3.1 Distributions of SO$_2$ and NO$_2$ tropospheric VCDs over the NCP

In this section, the distributions of SO$_2$ and NO$_2$ tropospheric VCDs over the NCP area are discussed using mobile DOAS observations. First, the overall distributions of SO$_2$ and NO$_2$ tropospheric VCDs along the measurement routes under different dominant winds are characterized. Furthermore, we analyze the spatial and temporal variation of SO$_2$ and NO$_2$ tropospheric VCDs along the southwest routes (Shijiazhuang–Baoding–Beijing) and southeast routes (Dezhou–Cangzhou–Tianjin–Beijing) for different wind fields. The possible transport route of trace gas is identified using these distribution characteristics.

Table 3. Both results measured using mobile DOAS and in situ instruments along the southwest and southeast routes for different wind fields.

VCD (molec. cm^{-2})		South wind	North wind	Ratio	Average
Southwest route	SO$_2$	6.09×10^{16}	2.35×10^{16}	2.69	4.22×10^{16}
	NO$_2$	2.16×10^{16}	1.22×10^{16}	1.77	1.69×10^{16}
Southeast route	SO$_2$	3.29×10^{16}	3.51×10^{16}	0.94	3.40×10^{16}
	NO$_2$	1.34×10^{16}	9.68×10^{15}	1.38	1.15×10^{16}
Near-surface concentration (ppb)		South wind	North wind	Ratio	Average
Southwest route	SO$_2$	10.78	8.69	1.24	9.74
	NO$_2$	130.55	92	1.42	111.28
Southeast route	SO$_2$	23.29	11.24	2.07	17.27
	NO$_2$	119.12	116.82	1.02	117.97

* Ratio: defined as the value under southerly wind/northerly wind.
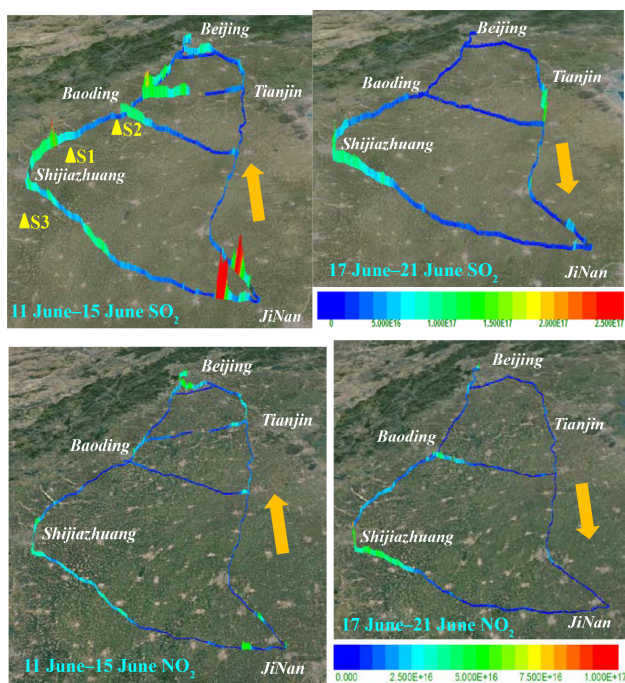
Figure 4. Spatial distributions of SO$_2$ and NO$_2$ VCDs over the NCP area for north (17–21 June) and south (11–15 June) wind fields. The orange arrows show the dominant wind direction; the yellow triangles show three different locations of main SO$_2$ sources in the southwest of the measurement region.

3.1.1 Overall distributions of SO$_2$ and NO$_2$ tropospheric VCDs

Each cycle measurement takes 4 to 5 days to complete, and this can lead to the measured air mass change when meteorological conditions vary rapidly. However, as described in Sect. 2.3 and listed in Table 1, the dominant wind field as a main influencing factor in air mass variation has not significantly changed, particularly the dominant wind direction of southerly and northerly winds during the measurement periods for mobile DOAS. However, air mass variation can also be affected by some other factors (e.g., temperature, humidity, and pressure, as discussed in Sect. 2.1), though the atmospheric physical reaction processes are too complicated to discuss in this study. Thus, we assume that, in this work, the air mass does not change dramatically for each cycle measurement.

Typical spatial distributions of SO$_2$ and NO$_2$ VCDs along the measurement route over the NCP area for north and south wind fields are shown in Fig. 4. (The results for Cycle 3 and Cycle 4 are shown in Fig. S1.) The maps of SO$_2$ in Fig. 4 show that increased values are observed under southerly wind, particularly the results along the Taihang Mountains, which is also part of the southwest measurement route (Shijiazhuang–Baoding–Beijing). The high SO$_2$ VCDs detected in the region near the cities of Shijiazhuang and Baoding indicate that these regions have emission sources of SO$_2$. In addition, high SO$_2$ VCDs are also observed on the cross-section of the south route, particularly near the city of JiNan. This hot spot can always be found under southerly wind during the field campaign, suggesting a strong emission outside the measurement area and south of it. Based on the backward trajectory analysis, the big air pollution plume comes from the city of Liaocheng, which is another small city close to the western region of JiNan. Furthermore, relatively low SO$_2$ VCDs are observed along the southeast route compared with those of the southwest route.

However, for the northerly wind, no significant increased SO$_2$ VCDs are noted along the Taihang Mountains. The hot spots near JiNan are also less pronounced. The downwind SO$_2$ VCDs of the cities of Shijiazhuang and Tianjin are relatively high due to source emissions near the city. The results of comparison of wind direction from the south vs. north further suggest that the strong emission sources located at the southern region of the measurement area have a significant
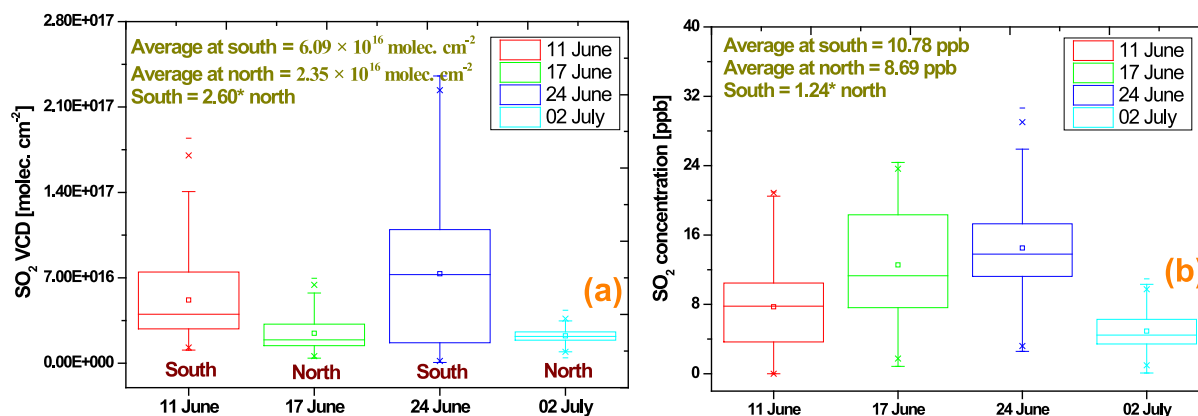
Figure 5. The SO$_2$ VCDs (**a**) and near-surface concentrations (**b**) along the southwest route.
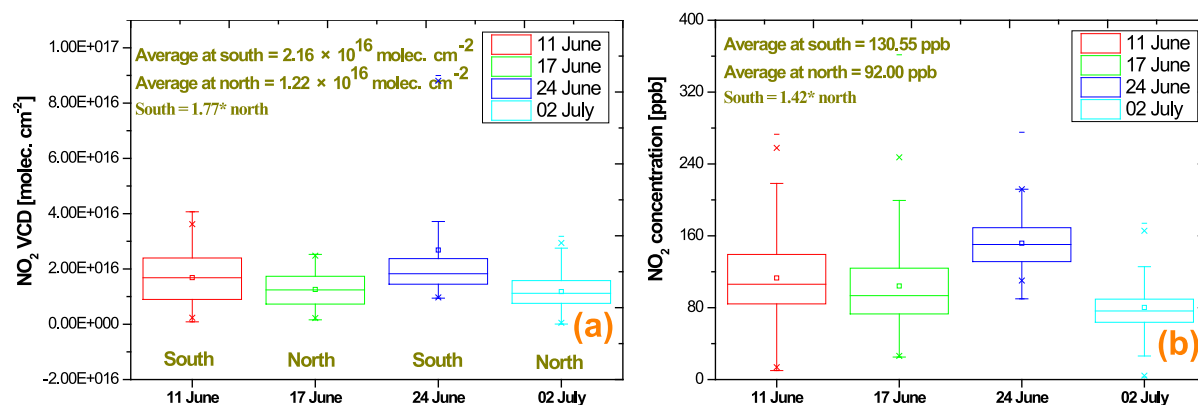

Figure 6. The NO$_2$ VCDs (**a**) and near-surface concentrations (**b**) along the southwest route.

influence on Beijing under southerly wind, particularly along the Taihang Mountains.

Unlike SO$_2$, no significant difference between the southerly and northerly wind for NO$_2$ VCDs is noted. The NO$_2$ VCDs are affected by local emissions within the cities. High NO$_2$ VCDs are obtained near Beijing, Baoding, Shijiazhuang, and Tianjin. The same is noted for SO$_2$, and due to strong emission source contributions, enhanced NO$_2$ VCDs are also found near JiNan for the south wind field.

3.1.2 Spatial and temporal variation of SO$_2$ and NO$_2$ along southwest and southeast routes under different wind fields

As detailed in the above analysis, the characteristics of SO$_2$ and NO$_2$ distributions have significant variation, including spatial and temporal differences along the southwest and southeast measurement routes. This section firstly investigates the SO$_2$ and NO$_2$ characteristics along southwest and southeast routes and then compares them with the results under southerly and northerly wind.

Table 3 lists the SO$_2$ and NO$_2$ VCDs from mobile DOAS and near-surface concentrations from in situ measurements under southerly and northerly wind along the southwest and southeast routes. For the southwest measurement route, the mean VCDs of SO$_2$ and NO$_2$ are 4.22×10^{16} and 1.69×10^{16} molec. cm^{-2}. The mean near-surface concentrations are 9.74 and 111.28 ppb for SO$_2$ and NO$_2$. For the southeast measurement route, the mean VCDs of SO$_2$ and NO$_2$ are 3.40×10^{16} and 1.15×10^{16} molec. cm^{-2}. The mean near-surface concentrations of SO$_2$ and NO$_2$ are 17.27 and 117.97 ppb, respectively. The VCDs along the southwest route are higher than that along the southeast route. However, the near-surface concentration along the different routes shows a reverse pattern.

The vertical column and in situ measurements are shown simultaneously in Table 3. It is interesting to note that such discussions can provide comprehensive information about surface emission and tropospheric pollution. We can also calculate the depth of a layer of air using the in situ mixing ratio and vertical column on the assumption of homogenous mixing within the planetary boundary layer (Chen et al., 2009). However, the height of the layer could not be estimated in
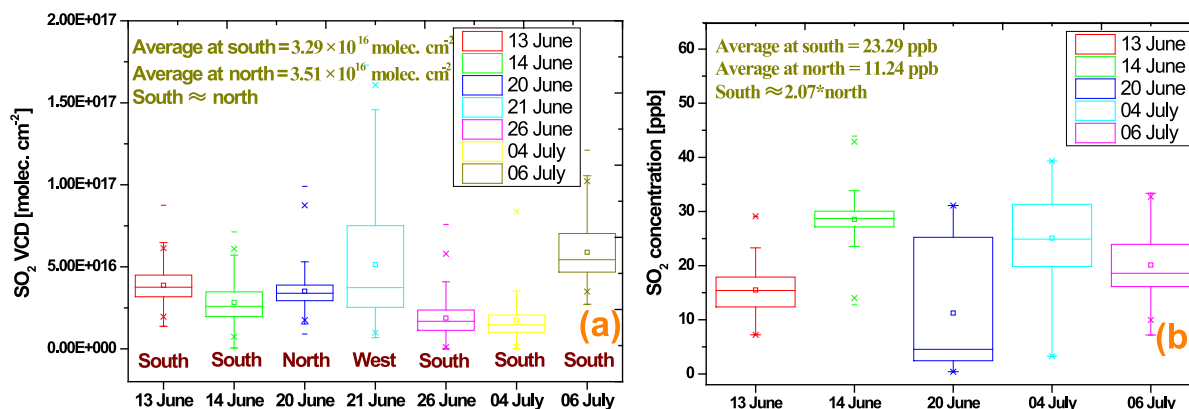
Figure 7. The SO_2 VCDs **(a)** and near-surface concentrations **(b)** along the southeast route; lack of near-surface data on 21 and 26 June due to instrument problems.
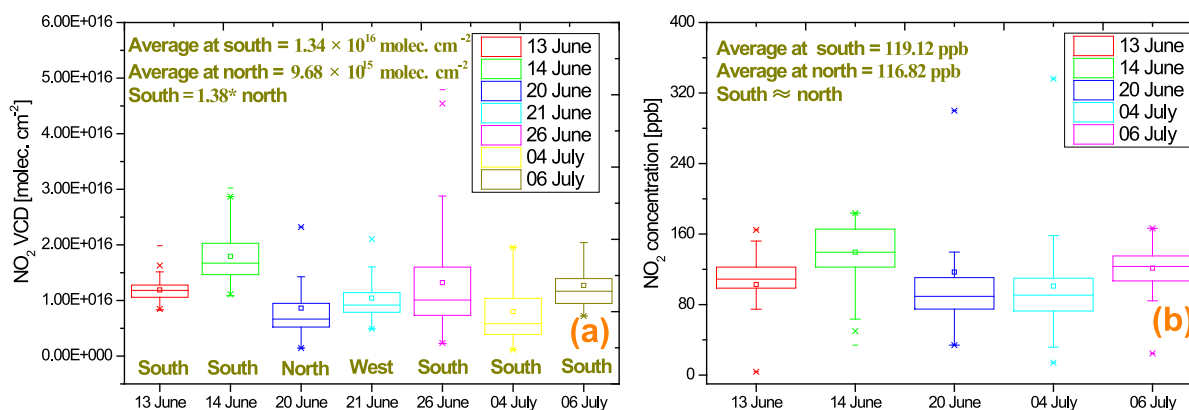

Figure 8. The NO_2 VCDs **(a)** and near-surface concentrations **(b)** along the southeast route; lack of near-surface data on 21 and 26 June due to instrument problems.

this way in this study because the in situ measurements were contaminated by very local vehicle emissions, especially for NO_2. Traffic exhaust is one of the major contributors to NO_2, and large traffic emissions result in the inhomogeneous mixing within the planetary boundary layer, so it is found that the NO_2 layer would be something like only 30 to 60 m thick using the above analysis method, which is very unreasonable compared to normal situations. In contrast, the SO_2 layer would vary from about 0.5 to 2.0 km thick, which is in the normal range.

The comparisons of VCDs between different wind fields show that the VCDs under southerly wind are much higher than those under northerly wind along the southwest route, particularly for SO_2, with the value of 6.09×10^{16} and 2.35×10^{16} molec. cm^{-2}. However, this phenomenon is not obvious along the southeast route. In addition, the comparisons of SO_2 near-surface concentration suggest that the difference between the different wind fields is less pronounced along the southwest route but is enhanced dramatically along

the southeast route under southerly wind, with the value of 23.29 ppb vs. 11.24 ppb under northerly wind.

3.1.3 Characterization of emission sources and identification of transport route

Both results from mobile DOAS and in situ instrument observations for each measurement day are shown in Figs. 5 to 8. According to the box chart plot, some distinct peak values of SO_2 VCDs are measured in the case of south wind, whereas this is not significant for SO_2 near-surface concentration, as shown in Fig. 5. These findings indicate that elevated sources existed in the southwest of the measurement region, and the elevated sources are the main SO_2 sources for this region. We could also infer that the high SO_2 value may be located in the upper layer. Moreover, we further investigate the potential locations of main SO_2 sources for this region. For the north wind, downwind peaks are found near Shijiazhuang, and thus sources of SO_2 within the encircled cycles, but closer to the southern measurement route, can be identified (S1 in Fig. 4). In addition, there is a slight increase
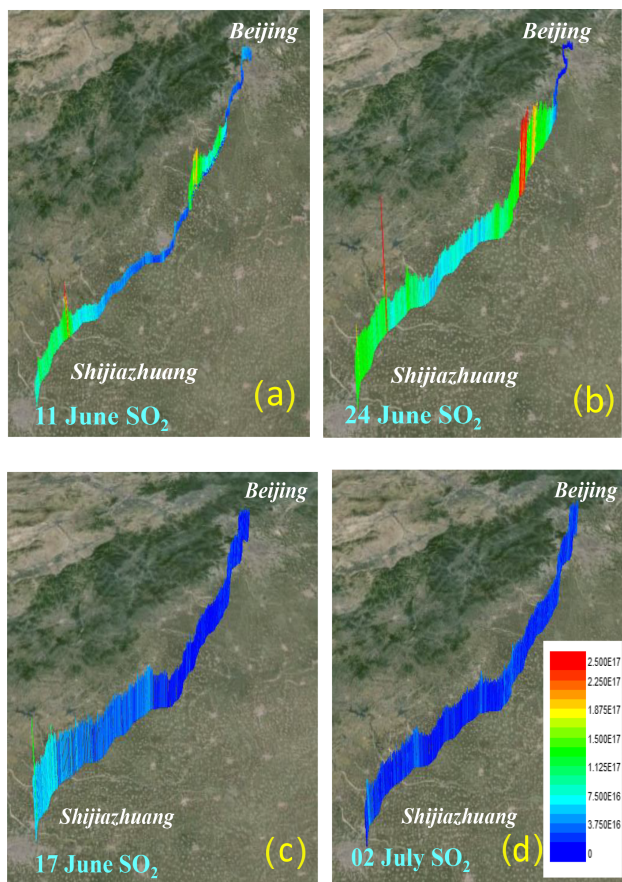
Figure 9. The variation of SO_2 VCDs along the southwest measurement routes (Beijing–Shijiazhuang) for south **(a, b)** and north **(c, d)** wind fields.

Figure 10. The mean concentrations of SO_2 measured at Gucheng (GC), Wanshou Xigong (GSXG), Tian Tan (TT), Guangyuan (GY), Fuyoujie (FYJ), Nongzhanguan (NZG), and AoTiZhongxin (ATZX) sites based on the south wind and north wind dominance in Beijing during the mobile DOAS observation period. The bars show the standard deviation (SD) of SO_2 concentrations.

in the southern region of Baoding; therefore we infer that a SO_2 source lies in the south of Baoding (S2 in Fig. 4). The maps for SO_2 in Fig. 4 show downwind peaks along the southwest measurement route when the wind comes from south, suggesting that important SO_2 emission sources are outside the cycles (S3 in Fig. 4). No significant peak values for NO_2 VCD (see Fig. 6) are noted. However, we found them on near-surface concentrations, such as on 11 June. The results show that the traffic emission located at the near surface is the main sources of NO_2. If we traverse areas with large volumes of vehicles, the NO_2 near-surface concentrations should increase.

For the southeast measurement routes, we did not observe the peak values of SO_2 VCDs and near-surface concentrations, as shown in Fig. 7. One interesting finding is that the SO_2 VCD on 21 June increased slightly from the box chart plot in Fig. 7. Through the analysis of the 24 h backward trajectory of 500 m on 21 June in the city of Cangzhou (the location of the peak value), we found that the air mass come from a west/southwest direction near mobile DOAS measurement time (near-surface wind direction dominated by west) but from a northeast direction when traced back a longer time in
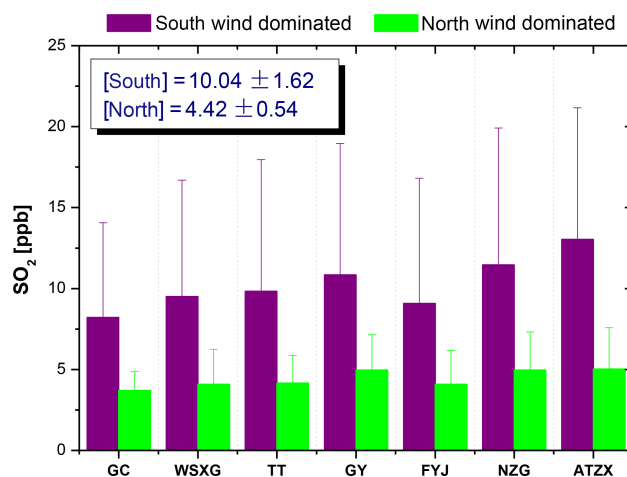
Cangzhou as shown in Fig. S2. So, we think that the higher SO_2 VCD on 21 June maybe caused by local emissions and transport from a northeast direction. In general, these findings verify that the low nonpoint sources are the main contributors in the southeast of the measurement region.

As shown in Fig. 8, the NO_2 VCDs for south wind are 1.38 times higher than those for north wind, but the near-surface concentrations are almost equal for these two different winds. The same is true for SO_2; we also did not find elevated NO_2 sources in the southeast of the measurement region.

Based on the above analysis, we could infer that pollution sources in the southwest and southeast regions consist of two types. This finding is also proven by the emission inventory: several large emission sources are located in the southwestern region, and some near-surface fugitive sources are located in the southeastern region (Wang et al., 2011).

Similar to SO_2, the average NO_2 VCD along the southeast route is lower than that along the southwest route, but the near-surface concentration is higher than that along the southwest route. The near-surface vehicle emissions are the major contributors of NO_2, and fugitive emission sources are additional sources of NO_2. In addition, the high NO_2 near-surface concentration along the southeast route indicates large traffic volume over this region. This is also consistent with the fact that the southeast route is an expressway from Beijing to Shanghai, the two most economically developed cities in China. Additionally, trade exchanges among these two and other cities are frequent.

The VCDs and near-surface concentrations of SO_2 and NO_2 are high under southerly wind in most cases, particularly for SO_2 VCDs along the southwest routes and SO_2 near-
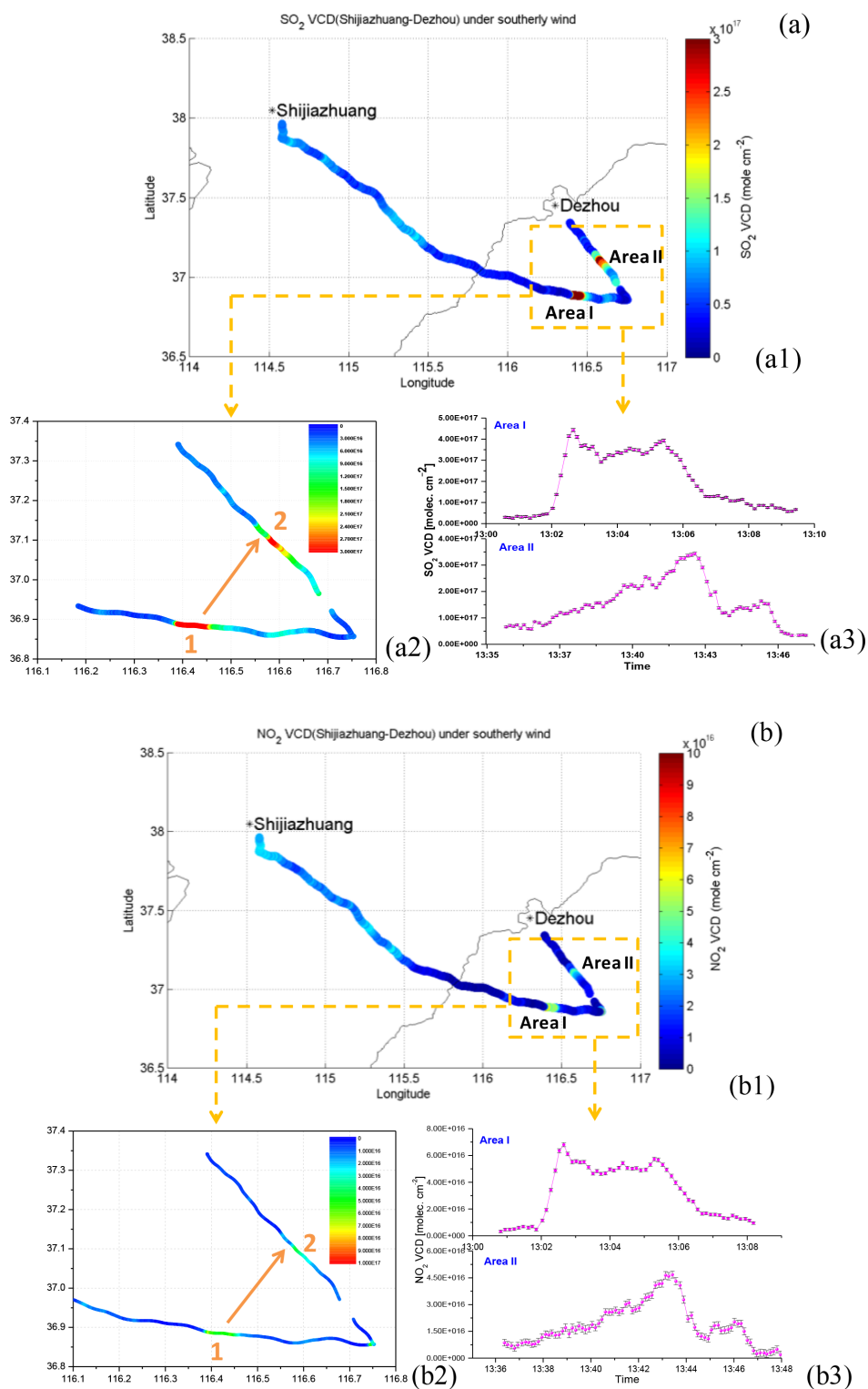
Figure 11. The hot spots of SO$_2$ **(a)** and NO$_2$ VCDs **(b)** are observed for the measurement of Shijiazhuang–Dezhou under southerly wind on 12 June. **(a1)**: Distribution of SO$_2$ VCDs along the whole measurement route; **(a2)** distribution of SO$_2$ VCDs in the hot spot area, where the origin arrow shows the diffusion of air mass from location 1 to location 2; **(a3)** time series of SO$_2$ VCDs for the polluted air mass for the rectangular area as shown in **(a1)**, where the top panel of **(a3)** shows Area I and the bottom shows Area II. Panels **(b1)**, **(b2)**, and **(b3)** are similar to **(a1)**, **(a2)**, and **(a3)**, only for NO$_2$.
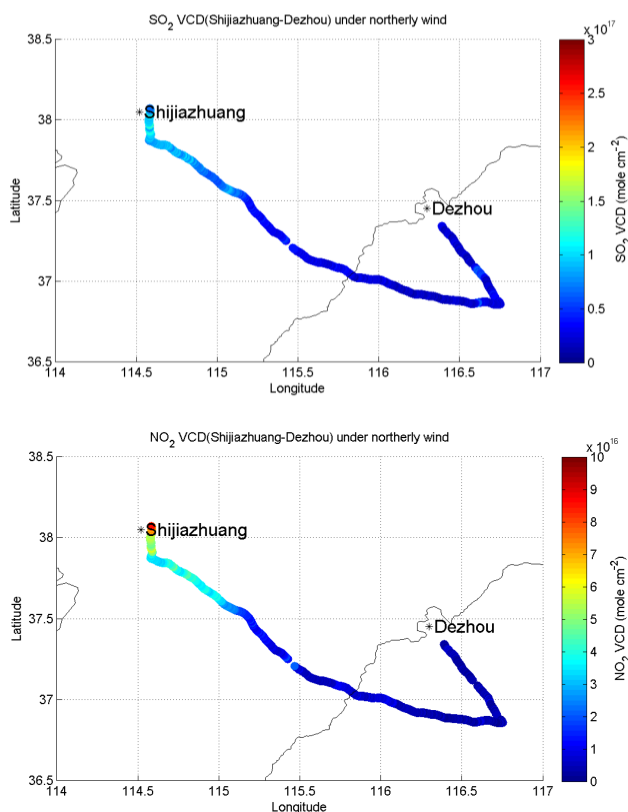
Figure 12. The distributions of SO$_2$ and NO$_2$ VCDs along the Shijiazhuang–Dezhou measurement route for northerly wind on 18 June.

surface concentrations along the southeast routes. From mobile DOAS observations, significant variation of SO$_2$ VCDs along the southwest routes (also along Taihang Mountains) was found, and this is shown in Fig. 9. The variation of SO$_2$ VCDs for different wind fields indicates that the southwest route is a transport route of SO$_2$ for Beijing. When the air plume comes from the south, the air quality in Beijing deteriorates. Figure 10 shows the mean SO$_2$ concentrations for the time when the south or north wind is dominant in Beijing. The monitoring data in seven state-controlled air-sampling sites demonstrate that the average SO$_2$ concentrations ranged from 8.22 to 13.04 ppb for south wind and from 3.71 to 5.02 ppb for north wind during the mobile DOAS observation period in the Beijing area. Previous studies also confirmed the presence of this transport route using other methods (Su et al., 2014). This work not only identifies the transport route of SO$_2$ using mobile DOAS observations, but it also determines the high SO$_2$ concentration existing in the upper layer in combination with the concurrent in situ data.

3.2 Analysis of hot spots

The hot spots are observed for the route of Shijiazhuang–Dezhou measurements under southerly wind. The maxi-

mum SO$_2$ VCD and NO$_2$ VCD can reach 4.84×10^{17} and 7.41×10^{16} molec. cm^{-2}. However, they are less pronounced for north wind. Figures 11 and 12 present the results of SO$_2$ and NO$_2$ VCDs for the Shijiazhuang–Dezhou measurements under southerly and northerly wind.

Figure 11 exhibits a large polluted air mass coming from the southern region in the rectangular area (Fig. 11a1 and b1) under the southerly wind on 12 June. First, this air mass led to the rapid enhancement of SO$_2$ and NO$_2$ VCDs in Area I and Location 1 (Fig. 11a1, a2, b1, and b2); then, the VCDs in Area II and Location 2 increased subsequently due to the air mass diffusion. The time series of SO$_2$ and NO$_2$ VCDs tell us that with the increase of distance, the peak value decreased in Area II and an observed width of air mass enlarged because of air mass diffusion. For Area I, the peak values of SO$_2$ and NO$_2$ VCDs are 4.43×10^{17} and 6.80×10^{16} molec. cm^{-2} at 13:02 LT. However, the peak values for SO$_2$ and NO$_2$ decreased to 3.44×10^{17} and 4.68×10^{16} molec. cm^{-2} in Area II at 13:43 LT.

Furthermore, observed widths of air mass are estimated in Area I and Area II from the time series of SO$_2$ VCDs in Fig. 10a3 using the following formula:

$$W = \sum_i (t_{i+1} - t_i) \cdot \overline{V}_{i+1 \to i}, \tag{2}$$

where i is the number of spectrum in Fig. 11a3, t_{i+1} and t_i are the time for the spectrum of i and $i+1$, and $\overline{V}_{i+1 \to i}$ is the mean car speed between t_{i+1} and t_i.

Using the above formula, the average observed width of air mass is calculated to be 11.83 km in Area I and 17.23 km in Area II. Combined with the observed widths for Areas I and II and the geometric relationships between these two locations, the distance of the air pollution sources from Area I is estimated to be approximately 61.39 km. The distance of Area I from Liaocheng is approximately 60 km, proving that the source is indeed from the direction of Liaocheng, as discussed in Sect. 3.1.1.

While the above peak values are less pronounced under the northerly wind on 18 June as shown in Fig. 12, this phenomenon further confirmed large sources located at the southern region outside the measurement area. When the dominant wind comes from the south, the air quality of the measurement area is severely influenced by the sources.

In addition, we simultaneously compare the results of the 1 min average VCDs with the 1 min near-surface concentrations along the Shijiazhuang–Dezhou routes. Figure 13 shows the time series of VCDs and near-surface concentrations for SO$_2$ and NO$_2$ along the measurement route under southerly and northerly wind. For the specific southerly wind, such as on 3 July, the high SO$_2$ and NO$_2$ VCDs were captured through mobile DOAS in the areas, as shown in Fig. 11a2 or b2 (the area marked with the rectangular box in Fig. 13). This also indicates that the polluted air mass contained high levels of SO$_2$ and NO$_2$. Furthermore, from the time series observations of SO$_2$ near-surface concentra-
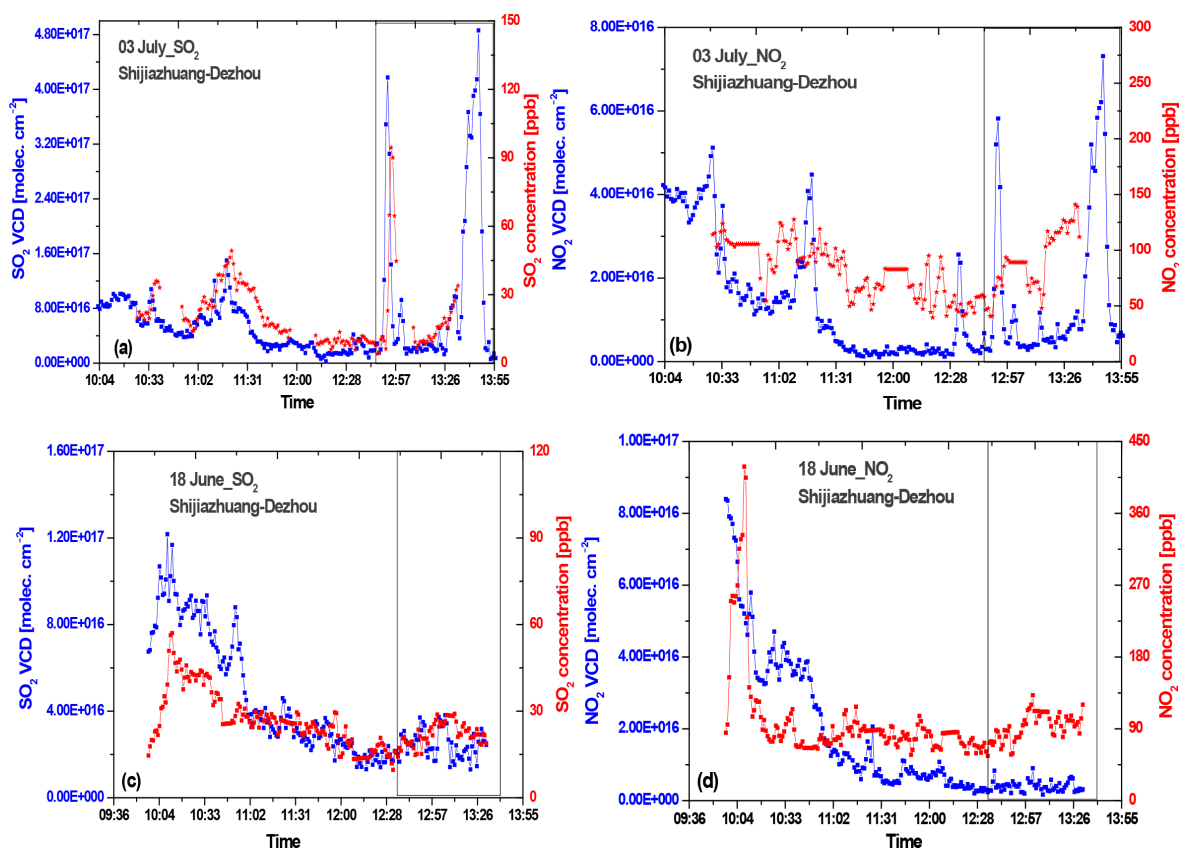
Figure 13. Time series of VCDs and near-surface concentrations of SO$_2$ and NO$_2$ along the route of Shijiazhuang–Dezhou for south and north wind. Panels **(a, b)** show SO$_2$ and NO$_2$ VCDs and near-surface concentrations on 3 July under southerly wind. Panels **(c, d)** show SO$_2$ and NO$_2$ VCDs and near-surface concentrations on 18 June under northerly wind. The rectangular boxes show polluted air mass area as shown in Fig. 11.

tions, high near-surface concentrations are observed simultaneously in the rectangle, as shown in Fig. 13a, and this is the same as SO$_2$ VCDs. The combined results demonstrate that part of the air mass has been deposited, resulting in the increase of SO$_2$ near-surface concentrations. However, one interesting thing has been found, namely that the NO$_2$ near-surface concentrations do not significantly increase in this area (Fig. 13b). Following the above explanation regarding SO$_2$, the declined air mass is supposed to cause an increase in NO$_2$ near-surface concentration. The lifetime of NO$_2$ is less than SO$_2$, and the NO$_2$ conversion to other species, such as nitrate, could account for this unexpected finding. For the northerly wind, both VCDs and near-surface concentrations do not increase obviously in the box area. The correlation analysis between NO$_2$ and CO near-surface concentrations (Fig. 14) shows that NO$_2$ near-surface concentration mainly results from vehicle exhaust, although the correlation coefficient under southerly wind is slightly better than that under northerly wind during the measurement periods.

3.3 Comparison with OMI NO$_2$

OMI is on board the Aura satellite of the Earth Observing System and was launched on 15 June 2004 with a nadir viewing mode (Levelt et al., 2006). OMI can be used to monitor global atmospheric NO$_2$ distribution with high spatial (up to 13×24 km) and temporal (daily global coverage) resolution. OMI is equipped with two charge-coupled devices spanning a wavelength range from 264 to 504 nm to measure spectra of scattered sunlight in the ultraviolet and visible spectra. The overpass time of OMI is 13:45 LT on the ascending node. In this study, the OMI tropospheric NO$_2$ data product from NASA is used. The data analysis consisted of three steps to derive tropospheric NO$_2$ VCDs. The SCDs of NO$_2$ are derived from OMI-collected spectra based on the DOAS method in the wavelength ranging from 405 to 465 nm. And then the AMFs are applied to convert the SCDs to VCDs with monthly average NO$_2$ profile shapes (Rotman et al., 2001). Finally, the stratospheric contribution is estimated to derive tropospheric NO$_2$ VCDs by subtracting the stratospheric columns. A detailed description of the tropospheric NO$_2$ retrieval process can be found in Bucsela et al. (2013).
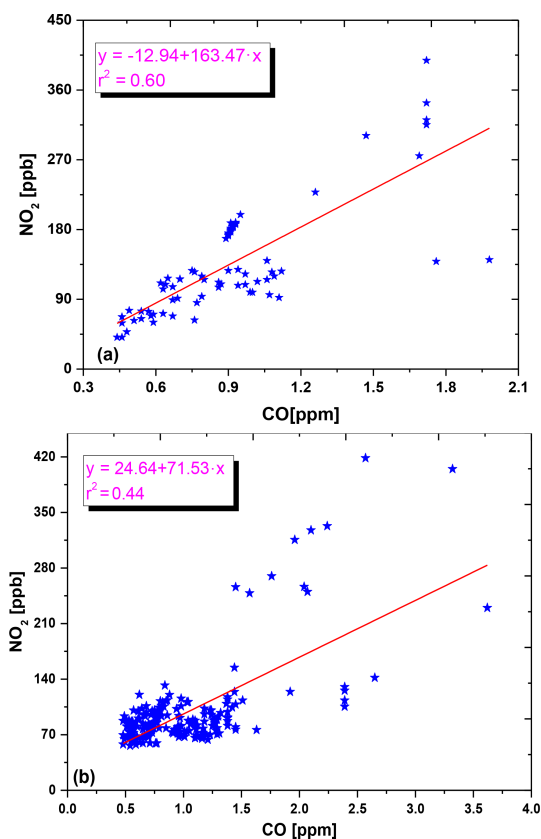
Figure 14. Correlation analysis between NO_2 and CO near-surface concentrations for the rectangle area as shown in Fig. 13; **(a)** south wind **(b)** north wind.

In this study, to achieve a better comparison between OMI and mobile DOAS, the OMI tropospheric NO_2 data are gridded onto a $0.1° \times 0.1°$ grid with an error and area-weighted gridding algorithm (Wenig et al., 2008). The cloud fraction of 0.4 is used as a threshold to filter out the data. As a result, a total of 8 days (11, 12, 13, 18, 25, and 26 June and 3 and 6 July with a cloud cover lower than 0.4) of measurements from both OMI and mobile DOAS can be used for data comparison.

The comparisons of NO_2 VCDs between both datasets for the 8-day measurement are shown in Fig. 15. Similar spatial patterns are detected by both OMI and mobile DOAS observations. In most cases, a high level of NO_2 VCD is observed around the Shijiazhuang area. However, the hot spots of mobile DOAS observations, as shown in Sect. 3.2, cannot be detected completely using OMI due to the insensitivity of OMI observations to near-surface sources. We also found from OMI observations that the NO_2 VCDs along the southwest route are higher than those along the southeast route, the same as discussed in Sect. 3.1.2.

Moreover, the mobile DOAS data are averaged within each gridded satellite pixel ($0.1° \times 0.1°$) and compared to OMI values within each pixel. The correlation analysis for all the

datasets of the 8-day measurements is shown in Fig. 16. The error bars indicate the OMI error and the standard deviation (SD) of mobile DOAS observations within the above pixels, which are also taken into account when performing the linear regression. The correlation coefficient (R^2) is 0.65, suggesting that both observations agree reasonably well. However, a systematic difference between the mobile DOAS and OMI NO_2 VCDs, implied by the fitted slope of 0.55, exists as shown in Fig. 16. These discrepancies can be attributed to source emissions from the near surface (e.g., traffic exhaust, industrial sources etc.) or lower troposphere (e.g., elevated sources). Due to the limited spatial resolution and shield by aerosols and clouds, the OMI observations are insensitive to these sources. However, mobile DOAS has the ability to respond rapidly to this, especially for the lower troposphere, like elevated sources. Also, some studies have shown that OMI NO_2 VCDs are systematically smaller than mobile DOAS and MAX-DOAS observations over polluted areas (Shaiganfar et al., 2011; Chan et al., 2015). Of course, some other factors can also result in these differences, like the NO_2 diurnal cycle. Previous studies (Wu et al., 2013) have shown that the strong diurnal variation of NO_2 occurs between 10:00 and 11:00. In this study, our mobile DOAS measurements are carried out approximately from 10:00 to 14:00, and the OMI overpass time may be 13:45. As a result, the time mismatch between OMI and NO_2 could result in different NO_2 VCDs. In addition, the NO_2 VCDs of OMI and mobile DOAS need to be converted from SCDs with AMFs. The calculations of AMFs should consider the trace gas profiles, aerosol profiles, ground albedo, and wavelength, etc. So, the different hypothesis for the calculation of AMFs can also yield different VCDs.

4   Conclusions

The NCP has been experiencing severe air pollution associated with an unprecedented economic boom and accelerated urbanization over the past few years. To characterize the temporal and spatial distributions and to investigate the effect of various sources on air quality, particularly for Beijing, the observations of tropospheric SO_2 and NO_2 VCDs through mobile DOAS are performed from 11 June to 7 July 2013.

Combined with the simultaneous measurements of near-surface concentrations through in situ instruments, the various temporal and spatial distributions of SO_2 and NO_2 under different wind fields are discussed. For the southwest measurement route, the mean SO_2 VCD under southerly wind is 6.09×10^{16} molec. cm^{-2}, which is 2.6 times higher than that for north wind (2.35×10^{16} molec. cm^{-2}). The near-surface SO_2 concentration under southerly wind is 1.24 times higher than that under northerly wind, with values of 10.78 and 8.69 ppb. Except for SO_2, the mean NO_2 VCD and near-surface NO_2 concentration under southerly wind are 1.77 and 1.42 times higher than those under northerly wind. The sig-
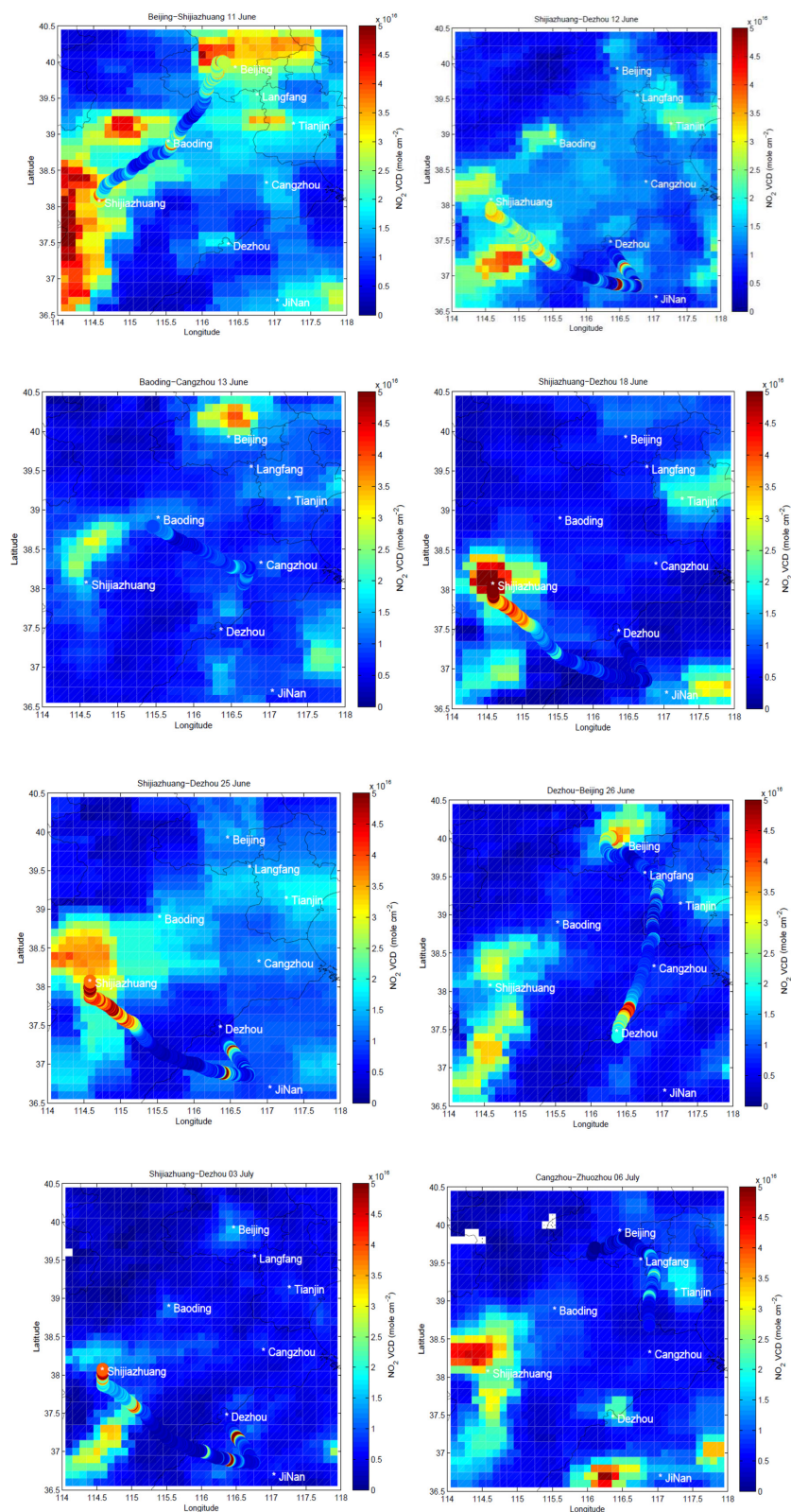
Figure 15. Spatial pattern of NO_2 measured through mobile DOAS and OMI. The header of each plot indicates the measured route and date, such as the first plot showing the result of the "Beijing–Shijiazhuang" route on 11 June. The color-coded circles indicate the mobile DOAS observations. The grid resolution of OMI was $0.1° \times 0.1°$.
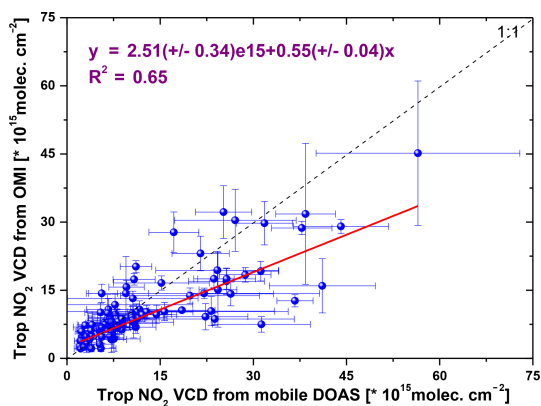
Figure 16. Correlation analysis of mobile DOAS and OMI NO$_2$ VCDs. The error bars show the OMI error and standard deviation (SD) of mobile DOAS as described in the text.

nificant discrepancies of SO$_2$ VCD between the two different wind fields indicate that the transport from the southern NCP area strongly affects the air quality over the northern NCP area (like Beijing). And the primary contributors to SO$_2$ in the southwest of the measurement region are elevated emission sources, like power plants and steel companies; this is evident through the use of the interrelated analysis of VCDs and in situ data. Moreover, the transport route of the path (Shijiazhuang–Baoding–Beijing) is identified.

However, for the southeast measurement route, we did not find a distinct difference of SO$_2$ VCDs under different wind fields, with values of 3.29×10^{16} and 3.51×10^{16} molec. cm^{-2} for south and north wind. The mean near-surface concentration of SO$_2$ for southerly wind is nearly double that of the value under northerly wind, with concentrations of 23.29 and 11.24 ppb. The NO$_2$ VCDs and near-surface concentrations along the southeast route also do not have significant variation. Under the south wind, the NO$_2$ VCD and near-surface concentration are 1.34×10^{16} molec. cm^{-2} and 119.12 ppb. Under the north wind, the NO$_2$ VCD and near-surface concentration are 9.68×10^{15} molec. cm^{-2} and 116.82 ppb. The higher SO$_2$ near-surface concentration along the southeast route indicates that the low area sources are the primary contributors to SO$_2$ rather than elevated sources.

Analysis of hot spot shows that the average observed width of air mass is 11.83 and 17.23 km associated with air mass diffusion. Another interesting finding is that the NO$_2$ near-surface concentration did not significantly enhance related to the area of air mass. The lifetime of NO$_2$ is less than that of SO$_2$, and NO$_2$ conversion to other species could account for this unexpected finding. The correlation analysis between NO$_2$ and CO near-surface concentrations shows that the NO$_2$ near-surface concentration mainly resulted from vehicle exhaust.

Furthermore, comparison with OMI NO$_2$ VCDs indicates a reasonable agreement between OMI and mobile DOAS with a correlation coefficient (R^2) of 0.65. Both datasets have

similar spatial patterns. In most cases, a high level of NO$_2$ VCDs is observed around the Shijiazhuang area. However, the fitted slope of 0.55 is significantly less than unity and may reflect the existence of some near-surface local sources, which correspond to insensitive observations or underestimation by OMI. This study will promote the development and extension of the mobile DOAS technique to rapidly capture the regional distribution of air pollutants, and it will promote the evaluation of the potential transport as well as the use of satellite validation.

The Supplement related to this article is available online at https://doi.org/10.5194/acp-18-1535-2018-supplement.

References

An, J. L., Li, J., Zhang, W., Chen, Y., Qu, Y., and Xiang, W. L.: Simulation of transboundary transport fluxes of air pollutants among Beijing, Tianjin, and Hebei Province of China, Acta Scientiae Circumstantiae, 32, 2684–2692, 2012.

Bogumil, K., Orphal, J., Homann, T., Voigt, S., Spietz, P., Fleischmann, O. C., Vogel, A., Hartmann, M., Kromminga, H., Bovensmann, H., Frerick, J., and Burrows, J. P.: Measurements of molecular absorption spectra with the SCIAMACHY preflight

model: instrument characterization and reference data for atmospheric remote-sensing in the 230–2380 nm region, J. Photoch. Photobio. A, 157, 167–184, 2003.

Boichu, M., Clarisse, L., Péré, J.-C., Herbin, H., Goloub, P., Thieuleux, F., Ducos, F., Clerbaux, C., and Tanré, D.: Temporal variations of flux and altitude of sulfur dioxide emissions during volcanic eruptions: implications for long-range dispersal of volcanic clouds, Atmos. Chem. Phys., 15, 8381–8400, https://doi.org/10.5194/acp-15-8381-2015, 2015.

Bucsela, E. J., Krotkov, N. A., Celarier, E. A., Lamsal, L. N., Swartz, W. H., Bhartia, P. K., Boersma, K. F., Veefkind, J. P., Gleason, J. F., and Pickering, K. E.: A new stratospheric and tropospheric NO$_2$ retrieval algorithm for nadir-viewing satellite instruments: applications to OMI, Atmos. Meas. Tech., 6, 2607–2626, https://doi.org/10.5194/amt-6-2607-2013, 2013.

Chan, K. L, Hartl, A., Lam, Y. F., Xie, P. H., Liu, W. Q., Cheung, H. M., Lampel, J., Pohlerf, D., Li, A., Xu, J., Zhou, H. J., Ning, Z., and Wenig, M. O.: Observations of tropospheric NO$_2$ using ground based MAX-DOAS and OMI measurements during the Shanghai World Expo 2010, Atmos. Environ., 119, 45–58, 2015.

Chen, D., Zhou, B., Beirle, S., Chen, L. M., and Wagner, T.: Tropospheric NO$_2$ column densities deduced from zenith-sky DOAS measurements in Shanghai, China, and their application to satellite validation, Atmos. Chem. Phys., 9, 3641–3662, https://doi.org/10.5194/acp-9-3641-2009, 2009.

Crutzen, P. J.: The influence of nitrogen oxides on the atmospheric ozone content, Q. J. Roy. Meteor. Soc., 96, 320–325, 1970.

Deutschmann, T., Beirle, S., Frieß, U., Grzegorski, M., Kern, C., Kritten, L., Platt, U., Prados-Roman, C., Pukite, J., Wagner, T., Werner, B., and Pfeilsticker, K.: The Monte Carlo atmospheric radiative transfer model McArtim: introduction and validation of Jacobians and 3-D features, J. Quant. Spectrosc. Ra., 112, 1119–1137, 2011.

Draxler, R. R. and Rolph, G. D.: Hysplit (hybrid single-particle lagrangian integrated trajectory) model access via noaa arl ready website, available at: https://ready.arl.noaa.gov/HYSPLIT.php, NOAA Air Resources Laboratory, 2003.

Finlayson-Pitts, B. J. and Pitts, J. N.: Chemistry of the Upper and Lower Atmosphere: Theory, Experiments, and Applications, Academic Press, San Diego, USA, 1999.

Guo, S., Hu, M., Misti, L. Z., Peng, J., Shang, D., Zheng, J., Du, Z., Wu, Z., Shao, M., Zeng, L., Mario, J. M., and Zhang, R.: Elucidating severe urban haze formation in China, P. Natl. Acad. Sci. USA, 111, 17373–17378, 2014.

Hönninger, G., von Friedeburg, C., and Platt, U.: Multi axis differential optical absorption spectroscopy (MAX-DOAS), Atmos. Chem. Phys., 4, 231–254, https://doi.org/10.5194/acp-4-231-2004, 2004.

Hu, J. L., Wang, Y. G., Ying, Q., and Zhang, H. L.: Spatial and temporal variability of PM$_{2.5}$ and PM$_{10}$ over the North China Plain and the Yangtze River Delta, China, Atmos. Environ., 95, 598–609, 2014.

Huang, R., Zhang, Y., Bozzetti, C., Kin-Fai, H., Cao, J., Han, Y., Daellenbach, K. R., Slowik, J. G., Platt, S. M., Canonaco, F., Zotter, P., RobertWolf, Simone, M. P., Emily, A. B., Monica, C., Giancarlo, C., Andrea, P., Margit, S., Gülcin, A., Jürgen, S. K., Ralf, Z., Zhisheng, A., Sönke, S., Urs, B., Imad, E. H., and Prévôt, A. S. H.: High secondary aerosol contribution to particu-

late pollution during haze events in China, Nature, 514, 218–222, 2014.

Ibrahim, O., Shaiganfar, R., Sinreich, R., Stein, T., Platt, U., and Wagner, T.: Car MAX-DOAS measurements around entire cities: quantification of NO$_x$ emissions from the cities of Mannheim and Ludwigshafen (Germany), Atmos. Meas. Tech., 3, 709–721, https://doi.org/10.5194/amt-3-709-2010, 2010.

Jang, M. and Kamens, R. M.: Characterization of secondary aerosol from the photooxidation of toluene in the presence of NO$_x$ and 1-propene, Environ. Sci. Technol., 35, 3626–3639, 2001.

Ji, D. S., Li, L., Wang, Y., Zhang, J., Cheng, M., Sun, Y., Liu, Z., Wang, L. L., Tang, G. Q., Hua, B., Chao, N., Wen, T., and Miao, H.: The heaviest particulate air-pollution episodes occurred in Northern China in January 2013: Insights gained from observation, Atmos. Environ., 92, 546–556, 2014.

Kanaya, Y., Irie, H., Takashima, H., Iwabuchi, H., Akimoto, H., Sudo, K., Gu, M., Chong, J., Kim, Y. J., Lee, H., Li, A., Si, F., Xu, J., Xie, P.-H., Liu, W.-Q., Dzhola, A., Postylyakov, O., Ivanov, V., Grechko, E., Terpugova, S., and Panchenko, M.: Long-term MAX-DOAS network observations of NO$_2$ in Russia and Asia (MADRAS) during the period 2007–2012: instrumentation, elucidation of climatology, and comparisons with OMI satellite observations and global model simulations, Atmos. Chem. Phys., 14, 7909–7927, https://doi.org/10.5194/acp-14-7909-2014, 2014.

Kraus, S.: DOASIS, A Framework Design for DOAS, PhD-thesis, University of Mannheim, Shaker Verlag, Heidelberg, Germany, 2006.

Kurucz, R. L., Furenlid, I., Brault, J., and Testerman, L.: Solar flux atlas from 296 nm to 1300 nm, National Solar Observatory Atlas No. 1, Office of University publisher, Harvard University, Cambridge, 1984.

Lee, H. L., Kim, Y. J., Jung, J., Lee, C., Klaus-Peter, H., Platt, U., Hu, M., and Zhu, T.: Spatial and temporal variations in NO$_2$ distributions over Beijing, China measured by imaging differential optical absorption spectroscopy, J. Environ. Manage., 90, 1814–1823, 2009.

Levelt, P. F., van den Oord, G. H. J., and Dobber, M. R.: The ozone monitoring instrument, IEEE T. Geosci. Remote, 44, 1093–1101, 2006.

Lv, L. H., Liu, W. Q., Zhang, T. S., Dong, Y. S., Chen, Z. Y., Fan, G. Q., Liu, Y., and Xiang, Y.: Characteristics of boundary layer height in Jing-Jin-Ji Area based on Lidar, Laser & Optoelectronics Progress, 54, 50–56, 2017 (in Chinese).

Ma, J. Z., Wang, W., Chen, Y., Liu, H. J., Yan, P., Ding, G. A., Wang, M. L., Sun, J., and Lelieveld, J.: The IPAC-NC field campaign: a pollution and oxidization pool in the lower atmosphere over Huabei, China, Atmos. Chem. Phys., 12, 3883–3908, https://doi.org/10.5194/acp-12-3883-2012, 2012.

Matsui, H., Koike, M., Kondo, Y., Takegawa, N., Kita, K., Miyazaki, Y., Hu, M., Chang, S.-Y., Blake, D. R., Fast, J. D., Zaveri, R. A., Streets, D. G., Zhang, Q., and Zhu, T., Spatial and temporal variations of aerosols around Beijing in summer 2006: Model evaluation and source apportionment, J. Geophys. Res., 114, D00G13, https://doi.org/10.1029/2008JD010906, 2009.

Meller, R. and Moortgat, G. K.: Temperature dependence of the absorption cross sections of formaldehyde between 223 and 323 K in the wavelength range 225–375 nm, J. Geophys. Res.-Atmos., 105, 7089–7101, https://doi.org/10.1029/1999JD901074, 2000.

Quan, J., Zhang, Q., He, H., Liu, J., Huang, M., and Jin, H.: Analysis of the formation of fog and haze in North China Plain (NCP), Atmos. Chem. Phys., 11, 8205–8214, https://doi.org/10.5194/acp-11-8205-2011, 2011.

Ramanathan, V. and Crutzen, P. J.: New directions: atmospheric brown "Clouds", Atmos. Environ., 37, 4033–4035, 2003.

Rotman, D. A., Tannahill, J. R., Kinnison, D. E., Connell, P. S., Bergmann, D., Proctor, D., Rodriguez, J. M., Lin, S. J., Rood, R. B., Prather, M. J., Rasch, P. J., Considine, D. B., Ramaroson, R., and Kawa, S. R.: Global modeling initiative assessment model: model description, integration, and testing of the transport shell, J. Geophys. Res.-Atmos., 106, 1669–1691, 2001.

Shaiganfar, R., Beirle, S., Sharma, M., Chauhan, A., Singh, R. P., and Wagner, T.: Estimation of NO_x emissions from Delhi using Car MAX-DOAS observations and comparison with OMI satellite data, Atmos. Chem. Phys., 11, 10871–10887, https://doi.org/10.5194/acp-11-10871-2011, 2011.

Su, F. Q., Gao, Q. X., Zhang, Z. G., Ren, Z. H., and Yang, X. X.: Transport pathways of pollutants from outside in atmosphere boundary layer, Research of Environmental Sciences, 17, 26–30, 2014 (in Chinese).

Sun, Y., Jiang, Q., Wang, Z., Fu, P., Li, J., Yang, T., and Yin, Y.: Investigation of the sources and evolution processes of severe haze pollution in Beijing in January 2013, J. Geophys. Res.-Atmos., 119, 4380–4398, https://doi.org/10.1002/2014JD021641, 2014.

Sun, Y. L., Wang, Z. F., Fu, P. Q., Yang, T., Jiang, Q., Dong, H. B., Li, J., and Jia, J. J.: Aerosol composition, sources and processes during wintertime in Beijing, China, Atmos. Chem. Phys., 13, 4577–4592, https://doi.org/10.5194/acp-13-4577-2013, 2013.

Shaiganfar, R., Beirle, S., Petetin, H., Zhang, Q., Beekmann, M., and Wagner, T.: New concepts for the comparison of tropospheric NO_2 column densities derived from car-MAX-DOAS observations, OMI satellite observations and the regional model CHIMERE during two MEGAPOLI campaigns in Paris 2009/10, Atmos. Meas. Tech., 8, 2827–2852, https://doi.org/10.5194/amt-8-2827-2015, 2015.

Thalman, R. and Volkamer, R.: Temperature dependent absorption cross-sections of O_2-O_2 collision pairs between 340 and 630 nm and at atmospherically relevant pressure., Phys. Chem. Chem. Phys., 15, 15371–15381, https://doi.org/10.1039/c3cp50968k, 2013.

van Donkelaar, A., Martin, R. V., Brauer, M., Kahn, R., Levy, R., Verduzco, C., and Villeneuve, P. J.: Global estimates of ambient fine particulate matter concentrations from satellite-based aerosol optical depth: development and application, Environ. Health Persp., 118, 847–855, 2010.

Vandaele, A. C., Hermans, C., Simon, P. C., Roozendael, M. V., Guilmot, J. M., Carleer, M., and Colin, R.: Fourier Transform measurement of NO_2 absorption cross-section in the visible range at room temperature, J. Atmos. Chem., 25, 289–305, 1996.

Wang, M., Zhu, T., Zheng, J., Zhang, R. Y., Zhang, S. Q., Xie, X. X., Han, Y. Q., and Li, Y.: Use of a mobile laboratory to evaluate changes in on-road air pollutants during the Beijing 2008 Summer Olympics, Atmos. Chem. Phys., 9, 8247–8263, https://doi.org/10.5194/acp-9-8247-2009, 2009.

Wang, M., Zhu, T., Zhang, J. P., Zhang, Q. H., Lin, W. W., Li, Y., and Wang, Z. F.: Using a mobile laboratory to characterize the distribution and transport of sulfur dioxide in and around Beijing, Atmos. Chem. Phys., 11, 11631–11645, https://doi.org/10.5194/acp-11-11631-2011, 2011.

Wang, S., Zhou, B., Wang, Z., Yang, S., Hao, N., Valks, P., Trautmann, T., and Chen, L.: Remote sensing of NO_2 emission from the central urban area of Shanghai (China) using the mobile DOAS technique, J. Geophys. Res., 117, D13305, https://doi.org/10.1029/2011JD016983, 2012.

Wang, Y. S., Yao, L., Wang, L. L., Liu, Z. R., Ji, D. S., Tang, G. Q., Zhang, J. K., Sun, Y., Hu, B., and Xin, J. Y.: Mechanism for the formation of the January 2013 heavy haze pollution episode over central and eastern China, Sci. China Earth Sci., 57, 14–25, https://doi.org/10.1007/s11430-013-4773-4, 2014.

Wang, Z. F., Li, J., Wang, Z., Yang, W. Y., Tang, X., Ge, B. Z., Yan, P. Z., Zhu, L. L., Chen, X. S., Chen, H. S., Wang, W., Li, J. J., Liu, B., Wang, X. Y., Wang, W., Zhao, Y. L., Lu, N., and Su, D. B.: Modeling study of regional severe hazes over mid-eastern China in January 2013 and its implications on pollution prevention and control, Sci. China Earth Sci., 57, 3–13, https://doi.org/10.1007/s11430-013-4793-0, 2014.

Wenig, M. O., Cede, A. M., Bucsela, E. J., Celarier, E. A., Boersma, K. F., Veefkind, J. P., Brinksma, E. J., Gleason, J. F., and Herman, J. R.: Validation of OMI tropospheric NO_2 column densities using direct-sun mode Brewer measurements at NASA Goddard Space Flight Center, J. Geophys. Res., 133, D16S45, https://doi.org/10.1029/2007JD008988, 2008.

World Health Organization: WHO Air Quality Guidelines for Particulate Matter, Ozone, Nitrogen Dioxide and Sulfur Dioxide Global Update 2005 Summary of Risk Assessment, Geneva, Switzerland, 2006.

Wu, Q. Z., Wang, Z. F., Gbaguidi, A., Gao, C., Li, L. N., and Wang, W.: A numerical study of contributions to air pollution in Beijing during CAREBeijing-2006, Atmos. Chem. Phys., 11, 5997–6011, https://doi.org/10.5194/acp-11-5997-2011, 2011.

Wu, F. C., Xie, P. H., Li, A., Chan, K. L., Hartl, A., Wang, Y., Si, F. Q., Zeng, Y., Qin, M., Xu, J., Liu, J. G., Liu, W. Q., and Wenig, M.: Observations of SO_2 and NO_2 by mobile DOAS in the Guangzhou eastern area during the Asian Games 2010, Atmos. Meas. Tech., 6, 2277–2292, https://doi.org/10.5194/amt-6-2277-2013, 2013.

Xu, X. P., Wang, L. H., and Niu, T. H.: Air pollution and its health effects in beijing, Ecosyst. Health, 4, 199–209, 1998.

Xu, J., Ma, J. Z., Zhang, X. L., Xu, X. B., Xu, X. F., Lin, W. L., Wang, Y., Meng, W., and Ma, Z. Q.: Measurements of ozone and its precursors in Beijing during summertime: impact of urban plumes on ozone pollution in downwind rural areas, Atmos. Chem. Phys., 11, 12241–12252, https://doi.org/10.5194/acp-11-12241-2011, 2011.

Yang, F., Tan, J., Zhao, Q., Du, Z., He, K., Ma, Y., Duan, F., Chen, G., and Zhao, Q.: Characteristics of $PM_{2.5}$ speciation in representative megacities and across China, Atmos. Chem. Phys., 11, 5207–5219, https://doi.org/10.5194/acp-11-5207-2011, 2011.

Ying, Q., Wu, L., and Zhang, H.: Local and inter-regional contributions to $PM_{2.5}$ nitrate and sulfate in China, Atmos. Environ., 94, 582–592, 2014.

Zhang, R., Jing, J., Tao, J., Hsu, S.-C., Wang, G., Cao, J., Lee, C. S. L., Zhu, L., Chen, Z., Zhao, Y., and Shen, Z.: Chemical characterization and source apportionment of $PM_{2.5}$ in Beijing: seasonal perspective, Atmos. Chem. Phys., 13, 7053–7074, https://doi.org/10.5194/acp-13-7053-2013, 2013.

Zhang, W., Zhu, T., Yang, W., Bai, Z., Sun, Y. L., Xu, Y., Yin, B., and Zhao, X.: Airborne measurements of gas and particle pollutants during CAREBeijing-2008, Atmos. Chem. Phys., 14, 301–316, https://doi.org/10.5194/acp-14-301-2014, 2014.

Zhao, B., Wang, S. X., Wang, J. D., Fu, J. S., Liu, T. H., Xu, J. Y., Fu, X., and Hao, J.: Impact of national NO$_x$ and SO$_2$ control policies on particulate matter pollution in China, Atmos. Environ., 77, 453–463, 2013.

Zhao, X. J., Zhao, P. S., Xu, J., Meng,, W., Pu, W. W., Dong, F., He, D., and Shi, Q. F.: Analysis of a winter regional haze event and its formation mechanism in the North China Plain, Atmos. Chem. Phys., 13, 5685–5696, https://doi.org/10.5194/acp-13-5685-2013, 2013.